DISCLAIMER

This report was prepared as an account of work sponsored by an agency of the United States Government. Neither the United States Government nor any agency thereof, nor any of their employees, makes any warranty, express or implied, or assumes any legal liability or responsibility for the accuracy, completeness, or usefulness of any information, apparatus, product, or process disclosed, or represents that its use would not infringe privately owned rights. Reference herein to any specific commercial product, process, or service by trade name, trademark, manufacturer, or otherwise does not necessarily constitute or imply its endorsement, recommendation, or favoring by the United States Government or any agency thereof. The views and opinions of authors expressed herein do not necessarily state or reflect those of the United States Government or any agency thereof. Reference herein to any social initiative (including but not limited to Diversity, Equity, and Inclusion (DEI); Community Benefits Plans (CBP); Justice 40; etc.) is made by the Author independent of any current requirement by the United States Government and does not constitute or imply endorsement, recommendation, or support by the United States Government or any agency thereof.

BNL-228037-2025-INRE

Decay spectroscopy of an isomeric state in 251Md

C. Morse

April 2025

Nuclear Science and Technology Department

Brookhaven National Laboratory

U.S. Department of Energy

USDOE Office of Science (SC), Nuclear Physics (NP)

DISCLAIMER

Decay spectroscopy of an isomeric state in ^{251}Md

C. Morse,[1,2] R.M. Clark,[2] D. Seweryniak,[3] C.J. Appleton,[2] C.M. Campbell,[2] M.P. Carpenter,[3] P. Chowdhury,[4] H.L. Crawford,[2] M. Cromaz,[2] P. Fallon,[2] Z. Favier,[5] T. Huang,[3,6] F.G. Kondev,[3] A. Korichi,[7] T. Lauritsen,[3] D.H. Potterveld,[3] W. Reviol,[3] D. Rudolph,[8] C. Santamaria,[2] G. Savard,[3] G.L. Wilson,[9] and S. Zhu[1,3,*]

[1]*National Nuclear Data Center, Brookhaven National Laboratory, Upton, NY 11973, USA*
[2]*Nuclear Science Division, Lawrence Berkeley National Laboratory, Berkeley, CA 94720, USA*
[3]*Physics Division, Argonne National Laboratory, Argonne, IL 60439, USA*
[4]*Department of Physics and Applied Physics, University of Massachusetts Lowell, Lowell, MA 01854, USA*
[5]*Physics Department, CERN, 1211 Geneva 23, Switzerland*
[6]*Institute of Modern Physics, Chinese Academy of Sciences, Lanzhou 730000, China*
[7]*IJCLab, Laboratoire de Physique des 2 Infinis Irène Joliot-Curie, Orsay IN2P3/CNRS France*
[8]*Department of Physics, Lund University, SE-22100 Lund, Sweden*
[9]*Department of Physics and Astronomy, Louisiana State University, Baton Rouge, LA 70803*

(Dated: February 18, 2025)

Excited states in ^{251}Md have been populated by decay of an isomeric state at $E_x \approx 1174$ keV and studied via delayed γ-ray spectroscopy. We observe the population of two rotational bands, one of which we identify as the Nilsson $\pi\frac{7}{2}[514]$ ground-state band and the other we propose is based on the $\pi\frac{9}{2}[624]$ configuration. From the observed decay pattern, we suggest that the isomer spin-parity is $\frac{23}{2}^+$, with the three-quasiparticle configuration $\pi\frac{7}{2}[514] \otimes \left\{\nu\frac{7}{2}[624] \otimes \nu\frac{9}{2}[734]\right\}_{K^\pi=8^-}$. We compare our results to theoretical predictions of the single- and multi-quasiparticle structure of ^{251}Md.

I. INTRODUCTION

Superheavy elements ($Z \geq 104$) owe their existence to quantum shell effects which stabilize them against fission [1]. Experimental studies of their structure are challenging, and only recently has direct information begun to emerge [2]. Meanwhile, the comparative ease of producing the transfermium nuclei offers an alternative approach. These nuclei are well-deformed ($\beta_2 \approx 0.28$ [3–5]) owing to the existence of deformed gaps in the single-particle spectrum near $Z = 100$ and $N = 152$. Because of this, the proton orbitals near the Fermi surface in this region are expected to originate from the spherical subshells which define the shell gaps near $Z = 114$ [6]. In this sense, the transfermium nuclei act as a testing ground for theoretical models used to describe the superheavy region. Deformed odd-mass nuclei are of particular interest since they can provide direct insight into the single-particle structure.

In the present article, we report new results concerning the excited states of the odd-Z nucleus $^{251}_{101}$Md. Previous α-decay studies suggested that the ground state has the Nilsson configuration $\pi\frac{7}{2}[514]$, with an excited single-particle state based on the $\pi\frac{1}{2}[521]$ configuration located at about 55 keV [7, 8]. A subsequent in-beam γ-ray study identified a rotational band consistent with one signature of this $\pi\frac{1}{2}[521]$ configuration [9]. Very recently, the rotational band built on the $\pi\frac{7}{2}[514]$ configuration was identified through γ-ray and conversion-electron spectroscopy [10]. An isomer was also identified and interpreted as a high-K three-quasiparticle state, but it could not be placed precisely in the level scheme [11]. We present new data on the γ-ray transitions following decay of this isomer. We observe population of the rotational band built on the $\pi\frac{7}{2}[514]$ ground-state configuration, as well as transitions belonging to a new rotational band which we suggest is built on the $\pi\frac{9}{2}[624]$ configuration.

II. EXPERIMENTAL DETAILS

The experiment was performed at the Argonne Tandem Linear Accelerator System (ATLAS) at Argonne National Laboratory. A beam of $^{48}Ca^{11+}$ was accelerated to 216 MeV by ATLAS and delivered to the experimental area. For the first 60 hours, the beam current was slowly increased and had an average intensity of about 110 enA; thereafter, the current was held steady at an average intensity of 210 enA for about 105 hours. The beam was incident on a set of targets which were mounted on a wheel rotating at 800 rpm. The targets were composed of ≈ 0.45 mg/cm^2 ^{205}Tl, coated with a thin carbon layer on each side (≈ 10 μg/cm^2). The beam energy at the center of the target was calculated [12] to be approximately 214 MeV, which corresponds to the maximum cross section measured for the ^{205}Tl(^{48}Ca,2n)^{251}Md reaction [9]. The beam was swept across the width of the target segments with a frequency of a few hertz in order to distribute the intensity over their entire area. In addition, an electrostatic deflector was synchronized with the rotation of the target such that the beam was directed away from the spokes of the wheel.

The ^{251}Md fusion-evaporation residues recoiling out of the target were separated from the unreacted beam by the Argonne Gas-Filled Analyzer (AGFA). AGFA consists of a vertically-focusing quadrupole magnet followed

* Deceased

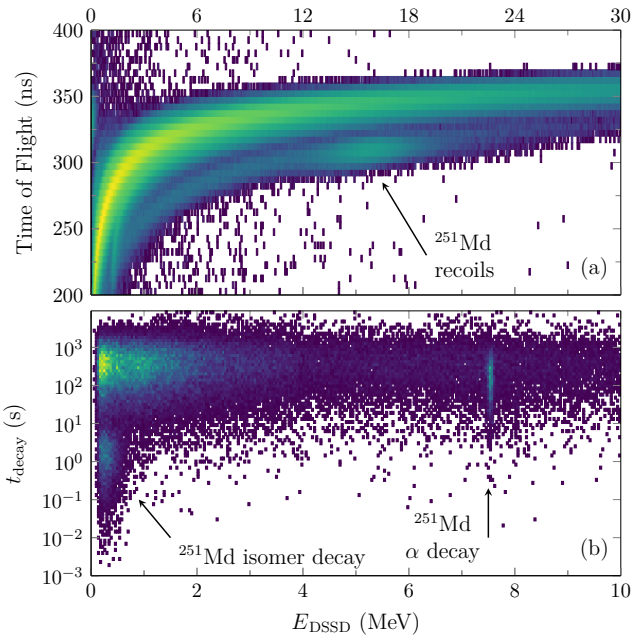

FIG. 1. (color online) (a) The particle-identification plot used to identify fusion-evaporation residues arriving at the focal-plane of AGFA. The vertical axis is the time of flight between the PGAC and the DSSD, while the horizontal axis shows the implantation energy in MeV. (b) The spectrum for the first generation of decays following a recoil implantation in a given pixel of the DSSD. The decay time is shown on the vertical axis, while the decay energy (in MeV) is shown on the horizontal axis. Features corresponding to α decay of the ground state of ^{251}Md and conversion electrons emitted in the decay of a known isomeric state are labeled.

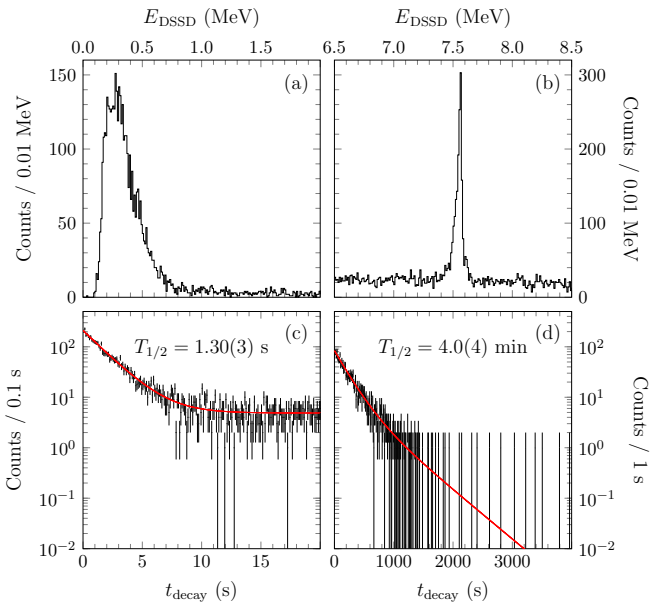

FIG. 2. (color online) (a) The energy distribution of low-energy events detected in the DSSD immediately following a recoil implantation, signifying the decay of a high-K isomer. (b) The same as (a) but for particles emitted in the decay of the ground state. (c) The time distribution of isomeric decays immediately following an implantation event. The half-life is extracted from a least-squares fit to the distribution, indicated by the red solid line. (d) The same as (c) but for the ground state. See text for details.

by a horizontally bending/focusing multi-function dipole magnet located 40 cm downstream from the target wheel. Helium gas was continuously flowed through the system at a pressure of $\approx$ 0.5 Torr in order to collapse the reaction-residue distribution to an average charge state. The helium was removed from the beam line upstream of the target via a differential-pumping setup. The magnet settings were selected to focus ^{251}Md residues onto the AGFA focal plane, while unreacted beam and other reaction products were directed into a beam dump approximately 1 m away.

The focal plane detectors of AGFA were used to identify ^{251}Md implantation and decay events. Fusion-evaporation residues were implanted into a 300-μm thick silicon double-sided strip detector (DSSD), with an active area of 64×64 mm. The DSSD was electrically segmented into 160 strips on the front and 160 orthogonal strips on the back, creating 25,600 pixels. Valid implantation and decay events required that both a front and a back strip registered a signal within a certain time interval. Adjacent strips which registered events sufficiently close in time were identified as charge-sharing, and recovered by assigning the sum of their energies to the strip which detected the higher energy. A Parallel-Grid Avalanche Counter (PGAC) was placed 20 cm upstream of the DSSD. The digital data acquisition system for the AGFA detectors is very similar to that of X-Array [13] (described later). A signal in the DSSD served as a trigger to the acquisition system to record data. For events in which signals were registered in both the PGAC and the DSSD, implantation events were identified based on the energy deposited in the DSSD and the time difference between the DSSD and the PGAC. This is shown in Fig. 1(a). An estimated 52,000 recoils were identified in this manner.

Once an implantation event was identified in a pixel of the DSSD, potential decay events occurring in the same pixel were correlated with that implant until another one was detected. Only events for which there was no signal in the PGAC and the energy deposited in the DSSD was less than 10 MeV were considered as possible decays. Figure 1(b) plots the time difference between the implantation event and the first decay event against the decay energy measured in the DSSD. The broad, horizontal distribution of events centered between 10^2-10^3 s on the vertical axis is due to random correlations after an implantation event. Superimposed on this background are decay events with an energy of about 7.55 MeV which corresponds to the known α-decay energy of the ground state of ^{251}Md [7]. There is also a collection of events

below 1 MeV which is a well-known signal of conversion electrons emitted following the decay of a high-K isomer.

The distributions of the energies for the isomer and α decay modes are shown in Fig. 2(a) and (b), respectively. The decay times for the isomer decay mode are restricted to less than 10 seconds in this plot. About 3600 events were identified as isomer decays, while approximately 2500 α decays were identified (1460 of which directly followed a recoil, corresponding to Fig. 2(b)). Given the 52,000 implants observed and a 50% efficiency to detect full-energy α events in the DSSD, this is consistent with the reported α-decay branching ratio $b_\alpha = 0.10(1)$ for the ^{251}Md ground state [7]. About 110 α decays were identified directly following decay of the isomer. The decay curves for the isomeric and ground states are shown in Figs. 2(c) and (d), respectively; the data in these plots are restricted to the first candidate decay following an implantation, and further restricted to have a detected energy either below 1 MeV for the isomeric state or between 7.45 and 7.65 MeV for the ground state. These distributions were fit with the function [14]

$$F(t) = ae^{-(\lambda+r)t} + be^{-rt}, \quad (1)$$

where λ is the decay constant of the state and r accounts for the random background. The resulting half-life for the ground state is $T_{1/2} = 4.0(4)$ min, consistent with previous measurements (4.28(12) min [11], 4.27(26) min [7]). The half-life of the isomeric state resulting from the fit is $T_{1/2} = 1.30(3)$ s, in agreement with the previous measurement of 1.4(3) s [11]. The uncertainty on the half-lives is only statistical.

About 20 decay events could be associated with α-decay of ^{249}Md (E_α = 8026 keV [15], $T_{1/2}$ = 24.8(10) s [16]), most likely produced through reactions on trace amounts of ^{203}Tl in the targets. Based on the reported cross sections and α-decay branching ratios for ^{251}Md ($\sigma = 760^{+180}_{-130}$ nb [9], $b_\alpha = 0.10(1)$ [7]) and ^{249}Md (σ = 300(80) nb, $b_\alpha = 0.75(5)$) [17], this is consistent with the ^{205}Tl targets having greater than 99% enrichment. Due to the small number of events, the production of ^{249}Md was otherwise neglected in the analysis.

Delayed γ rays emitted in coincidence with the decay of the ^{251}Md isomeric state were detected with the X-Array [13]. X-Array consists of five clover-type hyperpure germanium (HPGe) detectors, four of which have 60 mm × 60 mm crystals with the remaining "superclover" having 70 mm × 70 mm crystals. The superclover was placed behind the DSSD, in line with the beam path, while the remaining four clovers were arranged at 90° intervals around the beam axis with their faces in contact with the sides of the superclover. A similar arrangement is shown in Fig. 2 of Ref. [13]. During the present experiment, two of the smaller clovers were found to be malfunctioning and were turned off. The data acquisition system for X-Array was allowed to run independently of the AGFA data acquisition. Coincidences between the clover detectors and decay events in the AGFA DSSD were reconstructed in software based on their timestamps. Fig. 3 shows the γ-ray spectrum measured in coincidence with the decay of the isomer. Background γ rays outside of the time-coincidence window defined between the DSSD and X-Array were subtracted from this spectrum. Addback from neighboring germanium crystals was not used, as it was found to make minimal difference to the spectrum.

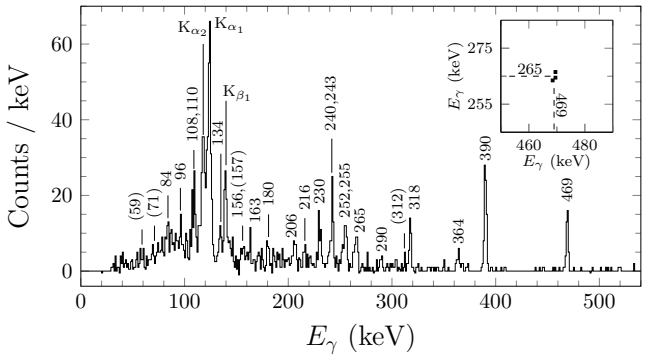

FIG. 3. The γ-ray spectrum measured in coincidence with the decay of the known isomeric state in ^{251}Md. Time-random events have been subtracted from the spectrum. Transition energies in keV are labeled, including X-rays. The energies in parentheses indicate possible transitions for which the statistics are insufficient to make a definite identification. The inset shows a portion of the $\gamma\gamma$ coincidence matrix, demonstrating that the 265-keV and 469-keV transitions are coincident.

A search was also performed for coincidences between time-correlated γ rays. Due to the low statistics, this search was mostly inconclusive. In the case of the 469-keV transition, however, three counts could be identified in an area with effectively no background. These events indicate that the 469-keV transition is in coincidence with the 265-keV transition. The three events are shown in the inset to Fig. 3.

III. ANALYSIS AND RESULTS

The decay scenario deduced from the present data is shown in Fig. 4. It has been constructed primarily based upon the γ-ray energies and intensities measured in the singles spectrum; Table I provides this information, with the intensities corrected for detector efficiency and normalized such that $I_\gamma = 100$ for the $E_\gamma = 390$-keV transition. The spin-parity assignments are tentative; parentheses indicate this in Fig. 4 and Table I, but are omitted in the remainder of the manuscript for readability. In this section, we will discuss several possible scenarios and demonstrate that the most consistent description of the data is as shown in Fig. 4.

The analysis relies on the intensity relations for γ rays in a rotational band. For convenience, we review these relations here. Within the rotational model [20], the tran-

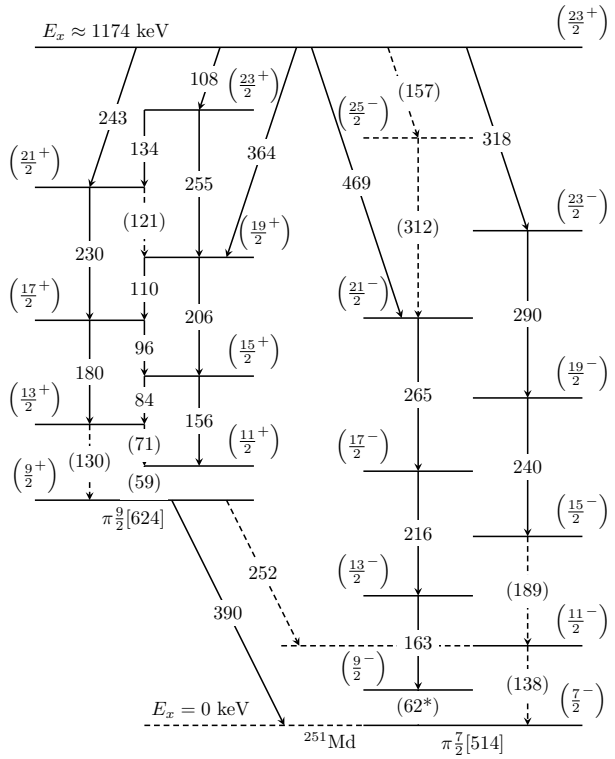

FIG. 4. The decay scenario constructed for the isomer in ^{251}Md based on the γ-ray transitions observed in the present work. Transitions in parentheses are the same ones that could not be definitively identified in Fig. 3. The dashed arrows indicate tentative placements, which include the unobserved γ rays and the 252-keV transition. The 62-keV energy for the $\left(\frac{9}{2}^-\right)$ level is taken from α spectroscopy [18]. All I^π assignments are tentative.

sition rates for $M1$ and $E2$ γ decay are given by

$$T(M1) = \frac{4}{3\hbar}\left(\frac{E_\gamma}{\hbar c}\right)^3 \langle I_i K 10 | I_f K\rangle^2 (g_k - g_R)^2 K^2 \mu_N^2, \tag{2}$$

$$T(E2) = \frac{1}{60\hbar}\left(\frac{E_\gamma}{\hbar c}\right)^5 \langle I_i K 20 | I_f K\rangle^2 e^2 Q_0^2, \tag{3}$$

where K is the projection of the angular momentum on the deformation axis, Q_0 is the electric quadrupole moment, g_k and g_R are the intrinsic and rotational gyromagnetic ratios, respectively, and the terms in angle brackets are Clebsch-Gordan coefficients. For a level with angular momentum $I_i = I$ which decays to levels with angular momenta $I_f = I-1$ and $I_f = I-2$, the ratio of the γ-ray intensities for the two transitions is given by

$$\frac{I_{\gamma_2}}{I_{\gamma_1}} = \frac{T(E2; I \to I-2)}{T(M1; I \to I-1) + T(E2; I \to I-1)}. \tag{4}$$

Using the definition of the mixing ratio for $\Delta I = 1$ transitions within a band, $\delta^2 = T(E2)/T(M1)$, one can combine Eqs. 2, 3, and 4 to find

$$\frac{\delta^2}{1+\delta^2} = \frac{2K^2(2I-1)}{(I+1)(I+K-1)(I-K-1)} \frac{I_{\gamma_2}}{I_{\gamma_1}} \left(\frac{E_{\gamma_1}}{E_{\gamma_2}}\right)^5, \tag{5}$$

$$\frac{g_k - g_R}{Q_0} = \sqrt{\frac{3}{20}} \frac{E_{\gamma_1} m_p}{\hbar^2} \frac{1}{|\delta|\sqrt{I^2-1}}, \tag{6}$$

where m_p is the proton mass. The value of g_k can be calculated using the asymptotic Nilsson quantum numbers

TABLE I. A summary of the γ-ray energies, intensities, and spin-parities of initial and final states based on the present work. The column labeled α provides the internal conversion coefficients [19] used to calculate the total $(\gamma + \epsilon)$ intensity. We have assumed the lowest allowed multipolarity for all γ rays, i.e. unmixed $M1$, $E1$, or $E2$ character.

E_γ (keV)	I_γ	$I_i^\pi \to I_f^\pi$	α	$I_{\gamma+\epsilon}$
83.7(6)	11(6)	$\left(\frac{15}{2}^+\right) \to \left(\frac{13}{2}^+\right)$	19.6(5)	227(124)
96.4(5)	9(5)	$\left(\frac{17}{2}^+\right) \to \left(\frac{15}{2}^+\right)$	13.0(3)	126(70)
107.5(6)	11(6)	$\left(\frac{23}{2}^+\right) \to \left(\frac{23}{2}^+\right)$	9.47(21)	115(63)
109.6(4)	20(7)	$\left(\frac{19}{2}^+\right) \to \left(\frac{17}{2}^+\right)$	8.95(16)	199(70)
134.4(4)	14(8)	$\left(\frac{23}{2}^+\right) \to \left(\frac{21}{2}^+\right)$	4.97(9)	84(48)
156.4(9)[a]	6(3)	$\left(\frac{15}{2}^+\right) \to \left(\frac{11}{2}^+\right)$	3.93(12)	30(15)
163.2(4)	8(3)	$\left(\frac{13}{2}^-\right) \to \left(\frac{9}{2}^-\right)$	3.29(6)	34(13)
180.4(4)	11(4)	$\left(\frac{17}{2}^+\right) \to \left(\frac{13}{2}^+\right)$	2.18(4)	35(13)
206.2(5)	14(5)	$\left(\frac{19}{2}^+\right) \to \left(\frac{15}{2}^+\right)$	1.283(22)	32(11)
215.8(5)	7(3)	$\left(\frac{17}{2}^-\right) \to \left(\frac{13}{2}^-\right)$	1.078(18)	15(6)
230.3(4)	31(7)	$\left(\frac{21}{2}^+\right) \to \left(\frac{17}{2}^+\right)$	0.845(13)	57(13)
239.6(6)	8(4)	$\left(\frac{19}{2}^-\right) \to \left(\frac{15}{2}^-\right)$	0.731(13)	14(7)
242.6(3)	37(7)	$\left(\frac{23}{2}^+\right) \to \left(\frac{21}{2}^+\right)$	4.07(6)	188(36)
252.4(5)[b]	11(4)	$\left(\frac{9}{2}^+\right) \to \left(\frac{11}{2}^-\right)$	0.0706(11)	12(4)
255.3(4)	27(6)	$\left(\frac{23}{2}^+\right) \to \left(\frac{19}{2}^+\right)$	0.582(9)	43(9)
265.3(4)	28(6)	$\left(\frac{21}{2}^-\right) \to \left(\frac{17}{2}^-\right)$	0.509(8)	42(9)
289.6(4)	8(3)	$\left(\frac{23}{2}^-\right) \to \left(\frac{19}{2}^-\right)$	0.378(6)	11(4)
317.7(3)	29(6)	$\left(\frac{23}{2}^+\right) \to \left(\frac{23}{2}^-\right)$	0.0437(7)	30(6)
364.0(4)	15(5)	$\left(\frac{23}{2}^+\right) \to \left(\frac{19}{2}^+\right)$	0.186(3)	18(6)
390.1(2)	100(13)	$\left(\frac{9}{2}^+\right) \to \left(\frac{7}{2}^-\right)$	0.0289(4)	103(13)
469.0(3)	56(11)	$\left(\frac{23}{2}^+\right) \to \left(\frac{21}{2}^-\right)$	0.0203(3)	57(11)

[a] Possible doublet with 157-keV $\left(\frac{23}{2}^+\right) \to \left(\frac{25}{2}^-\right)$

[b] Tentatively placed

according to the expression [21]

$$Kg_k = \sum(\Lambda g_\ell + \Sigma g_s), \tag{7}$$

where Λ and Σ are the projections of the nucleon orbital angular momentum and spin, respectively. For protons, $g_\ell = 1$ and $g_s^{\rm free} = 5.59$, with the latter value reduced by a factor of 0.6 as is typical [6, 17].

A. The $\pi\frac{7}{2}[514]$ band

Several of the γ rays visible in Fig. 3 have transition energies very similar to those assigned to the $\pi\frac{7}{2}[514]$ ground-state band in Ref. [10]. Three of these transitions were also observed in Ref. [11], at 216, 265, and 290 keV, and on this evidence it was tentatively suggested that the isomer feeds the ground-state band. We also observe a transition at 240 keV, although it is only partly resolved from another transition at 243 keV. We assign these transitions to the $\pi\frac{7}{2}[514]$ band.

The energies we observe are slightly higher than those of Ref. [10]. Based on a fit of the transition energies using the well-known rotational formula, we predict that the $\frac{11}{2}^- \rightarrow \frac{7}{2}^-$ and $\frac{9}{2}^- \rightarrow \frac{7}{2}^-$ transitions have energies of 137 keV and 62 keV, respectively. The latter is in agreement with Ref. [10] and also with the $\frac{9}{2}^-$ level energy reported in Ref. [18], but the former is several keV higher than Ref. [10]. In order to achieve a satisfactory fit to the data ($\chi^2/n = 1.3$), the term quadratic in $I(I+1)$ was included, with a linear coefficient of 6.92(2) keV and quadratic coefficient of -1.04(8) eV.

We place the prominent 469- and 318-keV γ rays depopulating the isomeric state and feeding the $\frac{21}{2}^-$ and $\frac{23}{2}^-$ states of the $\pi\frac{7}{2}[514]$ band, respectively. The inset to Fig. 3 establishes the coincidence between the 265- and 469-keV transitions. The $\frac{17}{2}^-$ level lies at about 440 keV, so the 469-keV γ ray must feed the $\frac{21}{2}^-$ state from above. This fixes the energy of the isomer relative to the ground-state rotational band. We estimate that the energy of the isomer is $E_x \approx 1174$ keV.

The decay pattern of the isomer into the $\pi\frac{7}{2}[514]$ band informs its possible spin-parity assignments. In particular, the parity of the isomer will strongly affect the transition intensities within the $\pi\frac{7}{2}[514]$ band. Explicitly, a positive parity for the isomer requires that the 469- and 318-keV transitions have $E1$ character, while negative parity would indicate $M1$ or $E2$ transitions with much larger conversion coefficients. Figure 5 compares these two scenarios (blue triangles for a positive-parity isomer, red squares for negative parity) with the experimental data (black circles). The γ-ray yields are calculated using Eqs. 5 and 6, while requiring that the transition intensity into and out of each level balances. Since only the $E2$ transitions are observed for this band, $g_k = 0.66$ was calculated using Eq. 7. We take $g_R = Z/A$, and adopt $Q_0 = 1330$ fm^2 based on calculations for several bands in ^{251}Md in Ref. [9]. The comparison favors an assignment of positive parity to the isomer[1]. Meanwhile, population of the $\pi\frac{7}{2}[514]$ band up to $\frac{23}{2}^-$ and non-observation of a transition to the $\frac{19}{2}^-$ state indicate that the spin of the isomer is likely greater than $\frac{21}{2}$, while an $E1$ character for the 469-keV transition requires that it be less than $\frac{25}{2}$. On the basis of these arguments, we assign $I^\pi = \frac{23}{2}^+$ to the isomeric state, which is also the conclusion of Ref. [11] on the basis of the most likely quasiparticle configuration.

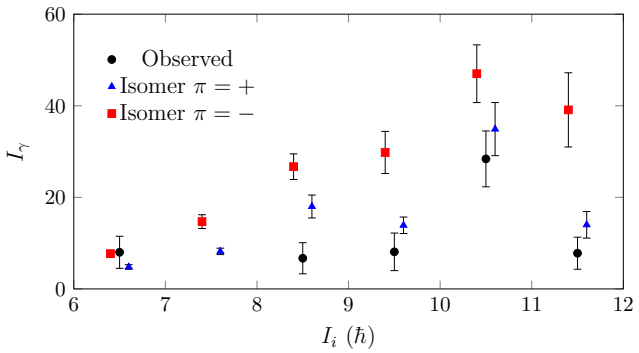

FIG. 5. (color online) A comparison between the observed $E2$ γ-ray intensities in the $\pi\frac{7}{2}[514]$ band (black circles) with those expected for an isomeric state with positive parity (blue triangles) or negative parity (red squares). The positive-parity assignment is preferred.

B. Identification of a $\frac{9}{2}^+$ band

Aside from the transitions which can be associated with the known $\pi\frac{7}{2}[514]$ band, several other transitions are visible in Fig. 3. These include low-energy transitions at 84, 96, 110, and 134 keV, which are all assumed to be of $M1$ character. There is also an excess of counts at about 121 keV. This cannot be explained by the well-known relative intensities of the K_α X-rays [22] but fits neatly with the proposed sequence of $M1$ transitions. Associated $E2$ transitions at 156, 180, 206, 230, and 255 keV are immediately identifiable in Fig. 3. Extrapolating below the observed $M1$ γ rays, there appear to be excess counts at approximately 59 and 71 keV, which would fit the sequence of transitions. These would be very highly converted, and we cannot positively identify them in the spectrum. Tentatively we place them as part of a new rotational band, acknowledging that further investigations are needed to verify their existence.

After assigning the aforementioned γ rays to this new band, a few transitions listed in Table I remain unplaced

[1] For a negative-parity isomer, we assume a stretched $E2$ character for the 469-keV transition for the purposes of this comparison. However, an $M1$ assignment would make the agreement with the data even worse.

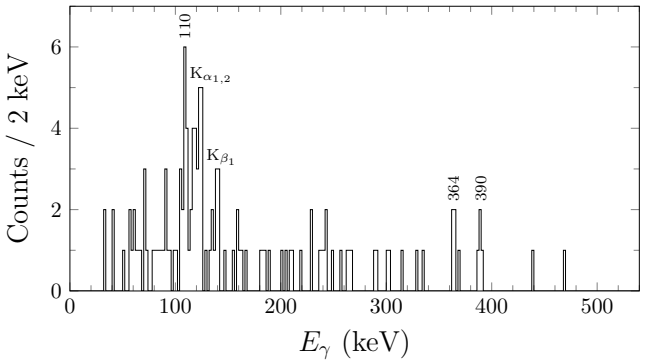

FIG. 6. The sum of coincidence spectra generated from the intraband γ rays placed as part of the new band identified in this work. In addition to X-rays, the 110-, 364-, and 390-keV transitions are apparent, which supports their placement populating or depopulating the new band.

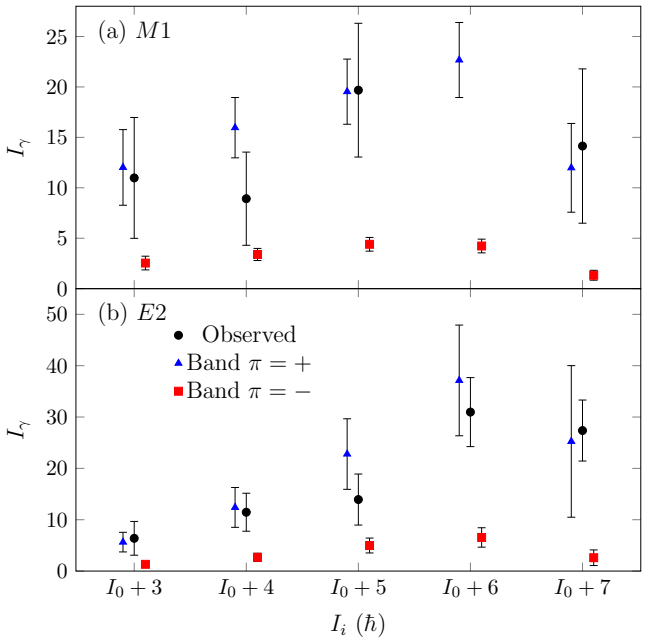

FIG. 7. (color online) The observed intensities of the (a) $M1$ and (b) $E2$ intraband transitions in the newly observed rotational band, indicated by the black circles, compared to the intensities expected if the band has positive parity (blue triangles) or negative parity (red squares). The latter can be excluded.

in Fig. 4. Notably, there are intense γ rays at 243, 364, and 390 keV. The energy difference between the 364-keV and the 243-keV γ rays is 121 keV, and we place these two transitions depopulating the isomer into the new band as shown in Fig. 4. The placement of the 134-keV and 255-keV transitions then requires that there be another transition out of the isomer, which according to the energy differences should be about 108 keV, only partly resolved from the 110-keV transition. Finally, there remain the transitions at 252 and 390 keV. Assuming that the 390-keV transition is the same one seen in prompt spectroscopy [10], it cannot originate directly from the isomer. Its large yield suggests that it instead depopulates the bottom of this new band. This fits well with the observed energy difference of the two rotational band heads, as shown in Fig. 4. We then tentatively place the 252-keV transition feeding the $\frac{11}{2}^-$ state in the ground-state band. The statistics are too low for individual coincidences within the new band to be identified, but a sum of the spectra generated by requiring coincidences between the intraband transitions is shown in Fig. 6. The appearance of the 110-, 364-, and 390-keV peaks support their placement in Fig. 4.

The parity of the newly established rotational band can be inferred by comparing the intraband transition intensities to those of the transitions from the isomeric state. Lacking a reason to invoke higher multipolarities, we assume that the 108-, 242- and 364-keV transitions have $E1$, $M1$, or $E2$ character. Figure 7 compares the observed intraband intensities (black circles) to the expected intensities for a positive-parity band fed by $M1$ and $E2$ transitions (blue triangles) or a negative-parity band fed by $E1$ transitions (red squares), calculated using Eqs. 5 and 6. Since we have not yet established the spins of the band members, we denote the level depopulated by the 390-keV transition as I_0. The comparison indicates a positive parity for the new band. It is important to note that, while we do not know *a priori* what value of K to use for the calculated intensities, any reasonable choice of K produces results similar to those shown in Fig. 7. This is due to the fact that the conversion coefficients for the transitions out of the isomer have the dominant effect on the overall intensities. We have used $K = \frac{9}{2}$ for the figure.

Having established that the new band likely has positive parity, the 364-keV transition is probably a stretched $E2$ transition, since there appears to be no direct population of the band below the level it feeds. That implies that this level has a spin-parity of $\frac{19}{2}^+$. As mentioned, the high intensity of the 390-keV γ ray indicates that it depopulates the bottom of the band. Together, these observations indicate that the band is built on a $\frac{9}{2}^+$ state, thus motivating our choice of K in Fig. 7. That the calculated intraband intensities agree with observation provides a measure of internal consistency to this assignment. In addition, the g-factors are expected to be constant for each member of a rotational band, and can be estimated from the $E2/M1$ intensity ratios. Table II provides the quantity $(g_k - g_R)/Q_0$ for the four levels in the band from which $E2$ and $M1$ transitions have been observed, along with the g_k value calculated using $Q_0 = 1330$ fm^2 [9] and $g_R = Z/A$. Despite the large uncertainties, the data points are consistent with each other.

TABLE II. Calculated g-factors determined from the present experimental data (top) and from the asymptotic Nilsson quantum numbers for various single-particle configurations using Eq. 7 (bottom).

I_i^π	$(g_k - g_R)/Q_o$ (fm^{-2})	g_k
$\frac{23}{2}^+$	$4.3(14) \times 10^{-4}$	0.97(19)
$\frac{19}{2}^+$	$5.3(14) \times 10^{-4}$	1.11(19)
$\frac{17}{2}^+$	$3.1(12) \times 10^{-4}$	0.82(16)
$\frac{15}{2}^+$	$3.6(16) \times 10^{-4}$	0.89(21)
Average	$4.1(7) \times 10^{-4}$	0.95(9)
Configuration		g_k
$\pi\frac{9}{2}[624]$		1.26
$\pi\frac{7}{2}[633]$		1.34
$\pi\frac{3}{2}[521]$		1.78
$\pi\frac{7}{2}[514]$		0.66
$\pi\frac{1}{2}[521]$		-1.35
$\pi\frac{5}{2}[512]$		1.47

C. The nature of the 390-keV transition

Curiously, the 390-keV γ ray, assigned as a $\frac{9}{2}^+ \rightarrow \frac{7}{2}^-$ pure $E1$ interband transition, has insufficient intensity to account for the full flux populating the $\frac{9}{2}^+$ band. The 252-keV transition, tentatively placed depopulating the $\frac{9}{2}^+$ level, has insufficient intensity to make up the difference. It is interesting to note that a 389-keV γ ray was observed under in-beam conditions, and that it was assigned $M2$ multipolarity on the basis of its K-shell conversion coefficient ($\alpha_K = 1.8(5)$) [10]. Assigning $M2$ character to the 390-keV transition observed in this work would result in a transition intensity which is larger than—but just consistent with—the observed feeding into the $\frac{9}{2}^+$ band. One could invoke a modest $E1$ admixture to improve the agreement. Nevertheless, such an assignment would be in tension with our suggested spin assignments, as it would be somewhat surprising for an $M2$ component to compete to this extent with an $E1$ transition.

Another possible explanation for the observed mismatch in intensity is that the conversion coefficient for the 390-keV $E1$ transition is anomalous. The conditions under which anomalous $E1$ internal conversion may arise are discussed in Ref. [23], which also gives examples. Additional instances are given in Appendix D of Ref. [6]. Inspection of the tables in these works show $E1$ conversion coefficients enhanced by factors of up to ~ 200, though factors of 2-20 are more typical. Among the heavy nuclei, the enhanced internal conversion coefficients for ^{245}Cm and ^{247}Cf in Ref. [6] seem relevant to the present discussion. We will argue in the next section that the most likely configuration for the new band in ^{251}Md is $\frac{9}{2}[624]$, and these transitions involve the same change in the asymptotic Nilsson quantum numbers. In that sense, they are useful analogues that may predict a similar enhancement in ^{251}Md. We are unable to distinguish between a mixed $E1/M2$ transition or an enhanced $E1$ conversion coefficient with the present data; it is possible that both scenarios apply. We simply wish to point out that the conversion coefficient data should be interpreted with caution, and the situation can only be resolved after future investigations.

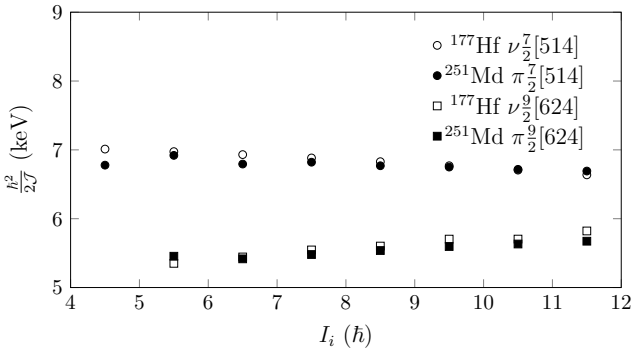

FIG. 8. A comparison of the moments of inertia for ^{251}Md (solid symbols) and ^{177}Hf (open symbols), with the latter scaled by a factor of $A^{-\frac{5}{3}}$. Circles indicate the $\pi\frac{7}{2}[514]$ band while squares represent the $\pi\frac{9}{2}[624]$ configuration in each nucleus. The correspondence is remarkable.

IV. DISCUSSION

Several single-particle orbitals are predicted to lie near the Fermi surface in ^{251}Md. Aside from the observed $\pi\frac{7}{2}[514]$ and $\pi\frac{1}{2}[521]$ orbitals, the $\pi\frac{3}{2}[521]$, $\pi\frac{5}{2}[512]$, $\pi\frac{7}{2}[633]$, and $\pi\frac{9}{2}[624]$ orbitals are expected to be present [6]. The band-head spin-parity of $\frac{9}{2}^+$ immediately suggests the $\pi\frac{9}{2}[624]$ configuration. The determination of positive parity for the new band rules out the $\pi\frac{3}{2}[521]$ and $\pi\frac{5}{2}[512]$ configurations. A $\pi\frac{7}{2}[633]$ assignment is possible, but requires invoking higher multipolarities for the linking transitions into and out of the band. The $\pi\frac{9}{2}[624]$ configuration is thus the most natural assignment to achieve a consistent description of the data. The g_k values calculated from Eq. 7 for the configurations listed above are given in the lower part of Table II. Of these, the $\pi\frac{9}{2}[624]$ configuration is close to the average of the experimental g_k values, with the $\pi\frac{7}{2}[633]$ configuration being very similar. However, the experimental value is not consistent within the uncertainty with any of the calculated values in Table II.

The transitions from the isomer into the rotational bands that we observe in this work are hindered by the large change in the K quantum number. This hindrance

TABLE III. Energies and K^π values of various one- and three-quasiparticle states calculated in the present work using a macroscopic-microscopic approach. The energies are expected to be accurate within about 200 keV. See text for details.

E_x (keV)	K^π	Configuration
0	$\frac{7}{2}^-$	$\pi\frac{7}{2}[514]$
60	$\frac{1}{2}^-$	$\pi\frac{1}{2}[521]$
320	$\frac{9}{2}^+$	$\pi\frac{9}{2}[624]$
370	$\frac{7}{2}^+$	$\pi\frac{7}{2}[633]$
390	$\frac{3}{2}^-$	$\pi\frac{3}{2}[521]$
1010	$\frac{23}{2}^+$	$\pi\frac{7}{2}[514]\otimes\left\{\nu\frac{7}{2}[624]\otimes\nu\frac{9}{2}[734]\right\}_{K^\pi=8^-}$
1070	$\frac{17}{2}^+$	$\pi\frac{1}{2}[514]\otimes\left\{\nu\frac{7}{2}[624]\otimes\nu\frac{9}{2}[734]\right\}_{K^\pi=8^-}$
1180	$\frac{15}{2}^+$	$\pi\frac{1}{2}[521]\otimes\pi\frac{7}{2}[633]\otimes\pi\frac{7}{2}[514]$
1440	$\frac{23}{2}^-$	$\pi\frac{7}{2}[633]\otimes\pi\frac{7}{2}[514]\otimes\pi\frac{9}{2}[624]$
1450	$\frac{19}{2}^+$	$\pi\frac{3}{2}[521]\otimes\pi\frac{7}{2}[514]\otimes\pi\frac{9}{2}[624]$
1480	$\frac{21}{2}^+$	$\pi\frac{7}{2}[514]\otimes\left\{\nu\frac{5}{2}[622]\otimes\nu\frac{9}{2}[734]\right\}_{K^\pi=7^-}$
1580	$\frac{15}{2}^+$	$\pi\frac{1}{2}[521]\otimes\left\{\nu\frac{5}{2}[622]\otimes\nu\frac{9}{2}[734]\right\}_{K^\pi=7^-}$
1750	$\frac{19}{2}^-$	$\pi\frac{7}{2}[514]\otimes\left\{\nu\frac{5}{2}[622]\otimes\nu\frac{7}{2}[624]\right\}_{K^\pi=6^+}$

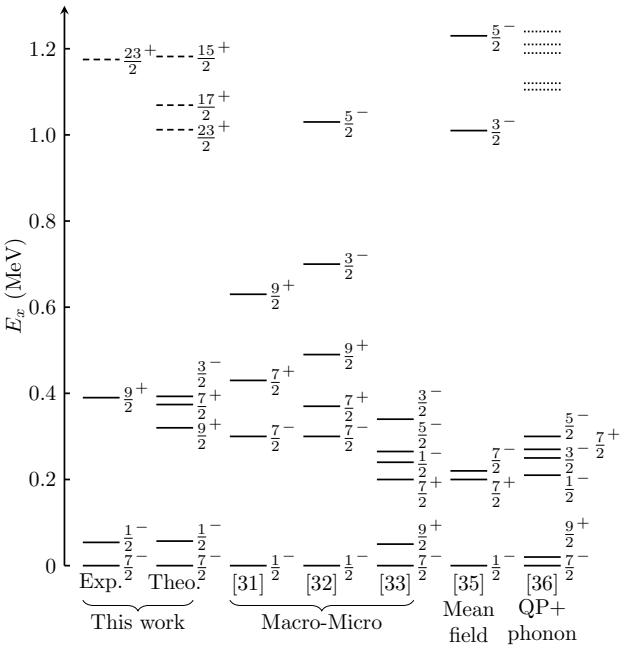

FIG. 9. A comparison between the experimental quasiparticle energies deduced in the present work (leftmost column) with various theoretical calculations (all other columns) up to about 1.2 MeV in excitation energy, with references given beneath. Single-quasiparticle states are indicated by solid lines, while dashed lines represent three-quasiparticle states. In the rightmost column, states with primarily phonon character are shown by dotted lines. See text for details.

can be quantified by the hindrance factor [24]

$$F_W = \frac{T_{1/2,\gamma}}{T^W_{1/2,\gamma}}, \tag{8}$$

where $T_{1/2,\gamma}$ is the partial half-life for γ decay for a given transition and $T^W_{1/2,\gamma}$ is the Weisskopf estimate for the partial half-life of the transition. This factor varies with both ΔK and the multipole order λ, and so it is often expressed in terms of the degree of forbiddenness $\nu = \Delta K - \lambda$ as the reduced hindrance factor $f_\nu = F_W^{1/\nu}$, which is typically of the order of 100 [25]. For the case of ^{251}Md, the calculated hindrance factors for the $E1$ transitions to the $\frac{7}{2}^-$ band have $f_\nu \approx 170$–180. The transitions to the $\frac{9}{2}^+$ band are in the range $f_\nu \approx 120$–150. All of these are fairly typical values, supporting the I^π assignments to the isomer and the bands it feeds.

There is only sparse information on rotational bands in neighboring odd-Z transfermium nuclei. However, a useful comparison can be made by looking to the $A \sim 180$ region where there are several examples of rotational bands based on neutron single-particle states with the same asymptotic Nilsson model quantum numbers as the proton states we assign in ^{251}Md. For instance, in ^{177}Hf—examined in detail in Ref. [20]—one finds a $\frac{23}{2}^+$ isomer decaying into rotational bands based on the $\nu\frac{7}{2}[514]$ and $\nu\frac{9}{2}[624]$ states. A comparison of the moments of inertia for these bands with the bands in ^{251}Md can be made by assuming similar deformations in the two mass regions and scaling by $A^{-5/3}$. As shown in Fig. 8, there is a remarkable similarity in the rotational properties for the two sets of states, lending further credence to the assignments that we have made for the bands in ^{251}Md.

A new macroscopic-microscopic calculation has been performed in order to predict the single- and multi-quasiparticle states in ^{251}Md. It is based on the Woods-Saxon potential with a universal parametrization [26]. The Lipkin-Nogami prescription [27] was used to describe pairing interactions, including blocking, and the energies of multi-quasiparticle states have been corrected by about 100 keV in order to account for residual spin-spin interactions. The results of the calculation are shown in Table III; the energies are expected to be accurate within about 200 keV, based on comparison of similar calculations with observed multi-quasiparticle states in other nuclei (e.g. Ref. [28, 29]). The results are also shown graphically in Fig. 9 in the column labeled "Theo.", which can be compared against the experimental data in the leftmost column. Single-quasiparticle states are indicated by solid lines, while dashed lines represent three-quasiparticle states. Overall, comparing the positions of the $\frac{9}{2}^+$ and $\frac{23}{2}^+$ states suggests that the calculated spectrum is slightly compressed, but still within 200 keV of the experimental results. On the basis of the excitation energy, both the predicted $\frac{7}{2}^+$ and $\frac{9}{2}^+$ states are reasonable candidates for the head of the rotational band we observe. Importantly, the calculation predicts that

the $\frac{23}{2}^+$ level is the lowest-lying multi-quasiparticle state and thus isomeric, in agreement with the experimental results. The configuration of this state in the calculation is $\pi\frac{7}{2}[514] \otimes \{\nu\frac{7}{2}[624] \otimes \nu\frac{9}{2}[734]\}_{K^\pi=8^-}$. This is in accord with the data for ^{250}Fm, in which a $K^\pi = 8^-$ isomer at $E_x = 1199$ keV was assigned the same two-quasineutron configuration [30]. The three-quasiparticle isomer in ^{251}Md can then be understood as an excitation of the ^{250}Fm core, with the unpaired proton remaining a spectator in the $\pi\frac{7}{2}[514]$ orbital.

In addition to our calculations, three other macroscopic-microscopic calculations are shown in the center columns of Fig. 9. A common feature of these calculations is an incorrect ordering of the quasiparticle levels. References [31, 32], both based on the Woods-Saxon potential, predict the $\frac{1}{2}^-$ state as the ground state, with the $\frac{7}{2}^-$ state several hundred keV above. Reference [33], which uses the two-center shell-model approach [34] to parametrize the nuclear shape, correctly places the $\frac{7}{2}^-$ state as the ground state, but inverts the $\frac{9}{2}^+$ and $\frac{1}{2}^-$ states compared to our experimental findings. These differences highlight the difficulty of simultaneously reproducing all of the observed properties of nuclei in this region.

Two self-consistent mean-field calculations using different effective interactions of the single-quasiparticle states in ^{251}Md have also been performed. One is based on the SLy4 interaction [35] and is given in Fig. 9, while the other uses the SLy5s1 [10] interaction but does not explicitly provide the quasiparticle energies. Both of these studies invert the ordering of the $\frac{1}{2}^-$ and $\frac{7}{2}^-$ states relative to experiment. They also place the $\frac{9}{2}^+$ state at about 1.5 MeV, much higher than our present experimental findings.

Finally, the right-most column of Fig. 9 shows a calculation using the quasiparticle-phonon model [36]. This calculation correctly predicts a $\frac{7}{2}^-$ ground state in ^{251}Md, but also inverts the $\frac{1}{2}^-$ and $\frac{9}{2}^+$ states relative to experiment. The states which have a significant phonon component, shown by dotted lines, are predicted to lie at a relatively high excitation energy compared to the single-quasiparticle states in this particular nucleus.

V. SUMMARY

In conclusion, we have reported on a measurement of the γ-ray spectrum following decay of the known isomer in ^{251}Md. Based on the γ-ray singles spectrum, and with support from the limited γ-γ coincidence data, we observe population of both the known $\pi\frac{7}{2}[514]$ rotational band and a new band which we propose to be built on the $\pi\frac{9}{2}[624]$ configuration. The present data indicate that the isomer spin-parity is likely $\frac{23}{2}^+$, with the configuration $\pi\frac{7}{2}[514] \otimes \left\{\nu\frac{7}{2}[624] \otimes \nu\frac{9}{2}[734]\right\}_{K^\pi=8^-}$. We have also performed a new microscopic-macroscopic calculation which reproduces the observed single- and multi-quasiparticle levels in this nucleus.

ACKNOWLEDGMENTS

The authors would like to thank A.O. Macchiavelli and S. Stolze for their assistance in conducting the experiment. This material is based upon work supported by the U.S. Department of Energy, Office of Science, Office of Nuclear Physics under Contract Nos. DE-AC02-98CH10886 (BNL), DE-AC02-05CH11231 (LBNL), DE-AC02-06CH11357 (ANL); Grant No. DE-FG02-94ER40848 (UML); the Knut and Alice Wallenberg Foundation (KAW 2015.0021); and the Wenner-Gren Foundations (SSv2020-0003). This research used resources of the ATLAS facility at ANL, which is a DOE Office of Science User Facility.

[1] V. M. Strutinsky, Nucl. Phys. A **95**, 420 (1967).
[2] A. Såmark-Roth *et al.*, Phys. Rev. Lett. **126**, 032503 (2021).
[3] P. Reiter *et al.*, Phys. Rev. Lett. **82**, 509 (1999).
[4] J. E. Bastin *et al.*, Phys. Rev. C **73**, 024308 (2006).
[5] R.-D. Herzberg *et al.*, Phys. Rev. C **65**, 014303 (2001).
[6] R. R. Chasman, I. Ahmad, A. M. Friedman, and J. R. Erskine, Rev. Mod. Phys. **49**, 833 (1977).
[7] A. Chatillon *et al.*, Eur. Phys. J. A **30**, 397 (2006).
[8] S. Antalic *et al.*, Eur. Phys. J. A **38**, 219 (2008).
[9] A. Chatillon *et al.*, Phys. Rev. Lett. **98**, 132503 (2007).
[10] R. Briselet *et al.*, Phys. Rev. C **102**, 014307 (2020).
[11] T. Goigoux *et al.*, Eur. Phys. J. A **57**, 321 (2021).
[12] O. B. Tarasov, D. Bazin, M. Hausmann, M. P. Kuchera, P. N. Ostroumov, M. Portillo, B. M. Sherrill, K. V. Tarasova, and T. Zhang, Nucl. Instrum. Methods Phys. Res. B **541**, 4 (2023).
[13] A. J. Mitchell *et al.*, Nucl. Instrum. Methods Phys. Res. A **763**, 232 (2014).
[14] M. E. Leino, S. Yashita, and A. Ghiorso, Phys. Rev. C **24**, 2370 (1981).
[15] C. D. Nesaraja, Nucl. Data Sheets **189**, 1 (2023).
[16] C. D. Nesaraja, Nucl. Data Sheets **195**, 718 (2024).
[17] R. Briselet *et al.*, Phys. Rev. C **99**, 024614 (2019).
[18] M. Asai, F. P. Heßberger, and A. Lopez-Martens, Nucl. Phys. A **944**, 308 (2015), special Issue on Superheavy Elements.
[19] T. Kibédi, T. W. Burrows, M. B. Trzhaskovskaya, P. M. Davidson, and C. W. Nestor, Jr, Nucl. Instrum. Methods Phys. Res. A **589**, 202 (2008).
[20] A. Bohr and B. R. Mottelson, *Nuclear Structure Vol. II* (World Scientific, Singapore, 1998).
[21] S. G. Nilsson, Dan. Mat. Fys. Medd. **29** (1955).

[22] R. B. Firestone, *Table of Isotopes: 1999 Update, 8th ed.*, edited by C. M. Baglin and S. Y. F. Chu (Wiley-Interscience, New York, 1999).

[23] S. G. Nilsson and J. O. Rasmussen, Nucl. Phys. **5**, 617 (1958).

[24] K. E. G. Löbner, Phys. Lett. B **26**, 369 (1968).

[25] F. G. Kondev, G. D. Dracoulis, and T. Kibédi, At. Data Nucl. Data Tables **103-104**, 50 (2015).

[26] S. Ćwiok, J. Dudek, W. Nazarewicz, J. Skalski, and T. Werner, Comput. Phys. Commun. **46**, 379 (1987).

[27] W. Nazarewicz, J. Dudek, R. Bengtsson, T. Bengtsson, and I. Ragnarsson, Nucl. Phys. A **435**, 397 (1985).

[28] H. M. David *et al.*, Phys. Rev. Lett. **115**, 132502 (2015).

[29] D. J. Hartley *et al.*, Phys. Rev. C **101**, 044301 (2020).

[30] P. T. Greenlees *et al.*, Phys. Rev. C **78**, 021303(R) (2008).

[31] S. Ćwiok, S. Hofmann, and W. Nazarewicz, Nucl. Phys. A **573**, 356 (1994).

[32] A. Parkhomenko and A. Sobiczewski, Acta Phys. Pol. B **35**, 2447 (2004).

[33] G. G. Adamian, N. V. Antonenko, S. N. Kuklin, and W. Scheid, Phys. Rev. C **82**, 054304 (2010).

[34] J. Maruhn and W. Greiner, Z. Phys. **251**, 431 (1972).

[35] M. Bender, P. Bonche, T. Duguet, and P.-H. Heenen, Nucl. Phys. A **723**, 354 (2003).

[36] N. Yu. Shirikova, A. V. Sushkov, and R. V. Jolos, Phys. Rev. C **88**, 064319 (2013).